CHAPTER 7

Efficient photocatalytic degradation of Rhodamine B by a novel CeO_2/Bi_2WO_6 composite film

Chapter seven describes the results, discussions and conclusions of CeO_2/Bi_2WO_6 composite film for Rhodamine B (RhB) degradation under visible light irradiation. As previously my published paper [1], the $0.4CeO_2/0.6Bi_2WO_6$ composite powder shows a high photocatalytic activity. Accordingly, we choose this ratio to fabricate film. The pure CeO_2, pure Bi_2WO_6 and $0.4CeO_2/0.6Bi_2WO_6$ composite films were prepared using a doctor blading method. The films were characterized for their physicochemical properties based upon X-ray Diffraction (XRD), Scanning Electron Microscopy (SEM), X-ray Photoelectron Spectroscopy (XPS), Photoluminescence (PL) and UV-vis Spectroscopy techniques. The photocatalytic activity of pure CeO_2, pure Bi_2WO_6 and $0.4CeO_2/0.6Bi_2WO_6$ composite films were examined by studying degradation of RhB under visible light irradiation.

7.1 Physical appearance

All films show the smooth surface with different color. The Bi_2WO_6 presents the pale yellow color of film, as shown in Figure 7.1a. The CeO_2 and $0.4CeO_2/0.6Bi_2WO_6$ composite films appear the light yellow color (Figure 7.1b) and pale yellow color (Figure 7.1c), respectively. The average weight of all samples was found to be 4-6 mg.

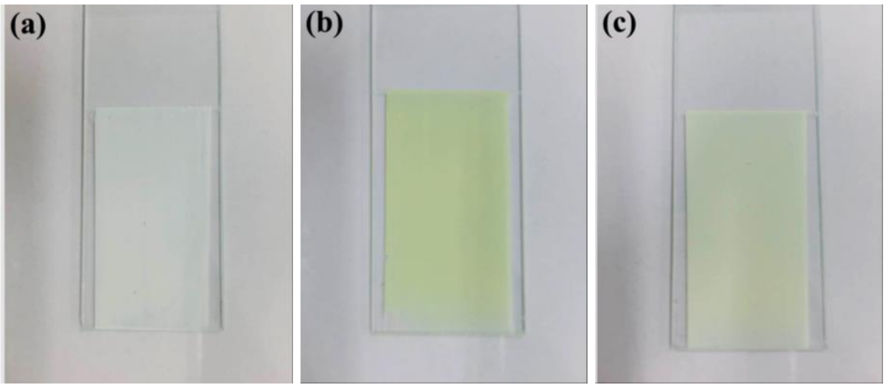

Figure 7.1 The physical appearance of (a) pure Bi_2WO_6, (b) pure CeO_2 and (c) $0.4CeO_2/0.6Bi_2WO_6$ films.

7.2 X-ray Diffraction (XRD)

The X-ray diffraction patterns of the one-layered Bi_2WO_6, CeO_2 and $0.4CeO_2/0.6Bi_2WO_6$ composite films are shown in Figure 7.2. The diffraction peaks of Bi_2WO_6 film are located at 2θ of 28.27°, 32.92°, 47.11° and 55.85°, which can be indicated as the (131), (002), (202) and (331) planes. The XRD peaks of Bi_2WO_6 film displayed orthorhombic phase conforming to JCPDS files no. 39-0256. The CeO_2 film exhibited a cubic fluorite phase with the diffraction peaks at 2θ of 28.45°, 33.06°, 47.43° and 56.04°, which can be identified by JCPDS files no. 34-0394 to the (111), (200), (220) and (311) planes. The $0.4CeO_2/0.6Bi_2WO_6$ composite film exposed the diffraction peaks of cubic fluorite and orthorhombic structure of CeO_2 and Bi_2WO_6, respectively. The average crystallite size of pure CeO_2, pure Bi_2WO_6 and $0.4CeO_2/0.6Bi_2WO_6$ composite films were calculated to be 4.30, 9.35 and 6.16 nm, respectively.

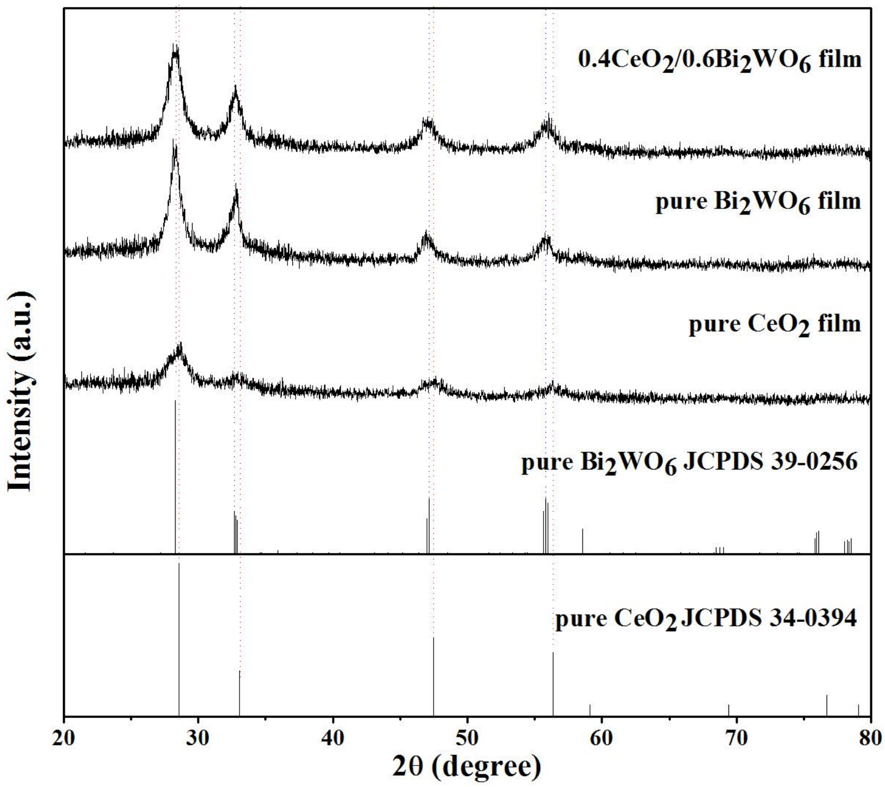

Figure 7.2 XRD patterns of pure Bi_2WO_6, pure CeO_2 and $0.4CeO_2/0.6Bi_2WO_6$ composite films.

7.3 Scanning Electron Microscopy (SEM)

Figure 7.3 shows the morphologies of pure CeO_2, pure Bi_2WO_6 and $0.4CeO_2/0.6Bi_2WO_6$ composite films. The one, two and three layers of pure CeO_2 film displayed a spherical-like particle with an average diameter in the range of 5-20 nm (Figure 7.3a-c). The morphology of Bi_2WO_6 film for one, two and three layers is presented in Figure 7.3d-f. SEM images of Bi_2WO_6 (1-3 layers) show a plate-like shape with the width in the range of 200-300 nm and length in the length of 300-700 nm. The $0.4CeO_2/0.6Bi_2WO_6$ composite film shows the spherical-like particle of pure CeO_2 and plate-like shape of pure Bi_2WO_6, as presented in Figure 7.3g-i. The cross-sectional images of pure CeO_2, pure Bi_2WO_6 and $0.4CeO_2/0.6Bi_2WO_6$ composite films in one, two and three layers are exhibited in Figure 7.4. The cross-sectional thickness of pure CeO_2 film increased with increasing the thickness layer from 1 layer to 3 layers. The thicknesses of CeO_2 in 1-3 layers were measured about 0.8-1.1 µm as shown in Figure 7.4a-c. The cross section of pure Bi_2WO_6 and $0.4CeO_2/0.6Bi_2WO_6$ composite films in

1-3 layers (Figure 7.4d-i) displayed the thickness in the range of 3-4 μm. The average thickness from three pieces of films in one, two and three layered of pure CeO_2, pure Bi_2WO_6 and $0.4CeO_2/0.6Bi_2WO_6$ films are observed in Figure 7.5. The thickness of the CeO_2 film is measured in the average range of 0.7, 1.0 and 1.3 μm for one, two and three layers, respectively. The Bi_2WO_6 and $0.4CeO_2/0.6\ Bi_2WO_6$ composite films were found the average thickness ranging from 3-4 μm.

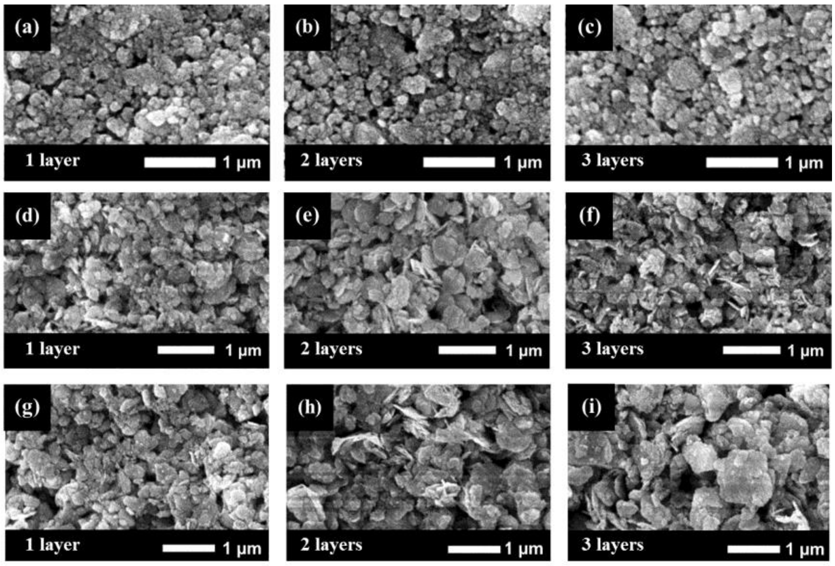

Figure 7.3 The morphological SEM images of (a-c) pure CeO_2, (d-f) pure Bi_2WO_6 and (g-i) $0.4CeO_2/0.6Bi_2WO_6$ composite films with the thickness of 1, 2 and 3 layers.

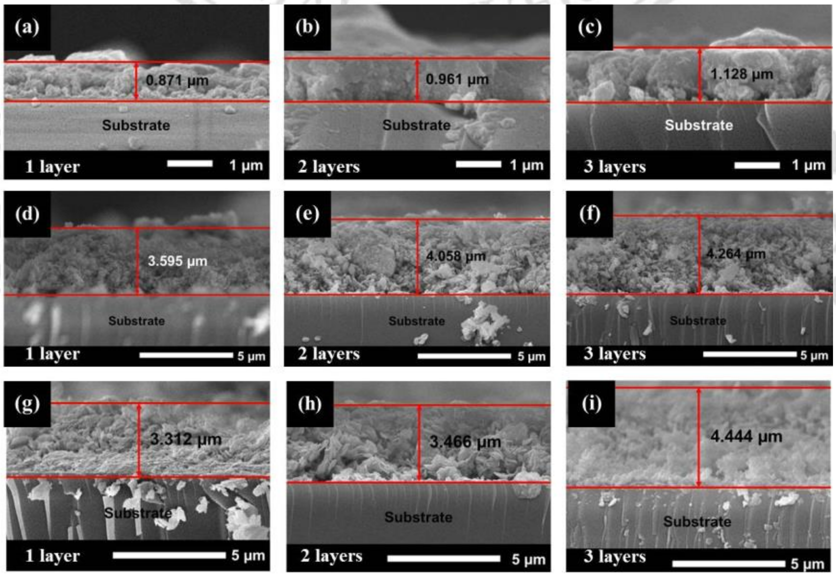

Figure 7.4 The cross-sectional SEM images of pure CeO_2 (a-c), pure Bi_2WO_6 (d-f) and $0.4CeO_2/0.6Bi_2WO_6$ composite (g-i) films with the thickness of 1, 2 and 3 layers.

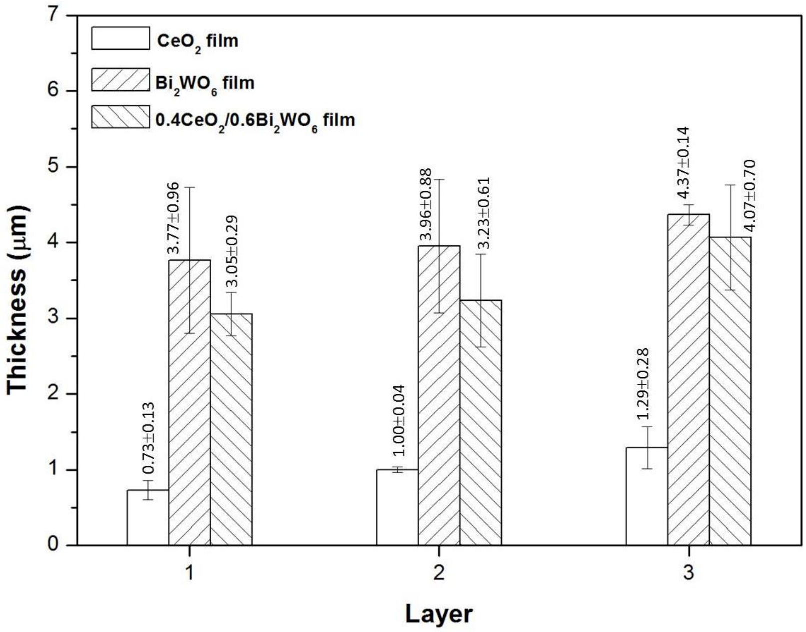

Figure 7.5 The average thickness of pure CeO_2, pure Bi_2WO_6 and $0.4CeO_2/0.6\ Bi_2WO_6$ composite films.

7.4 X-ray Photoelectron Spectroscopy (XPS)

The chemical states and element compositions of all films were investigated by X-ray photoelectron spectroscopy (XPS). The binding energies of Bismuth (Bi), Tungsten (W), Cerium (Ce) and Oxygen (O) are shown in Figure 7.6. The Bi $4f_{5/2}$ and Bi $4f_{7/2}$ peaks of pure Bi_2WO_6 and $0.4CeO_2/0.6Bi_2WO_6$ composite film are shown in Figure 7.6a. The main peaks of Bi $4f_{5/2}$ and Bi $4f_{7/2}$ were located at about 164.00 and 159.00 eV, which assigned to Bi^{3+} species in Bi_2WO_6 [2,3]. The binding energy peaks of 165.43 and 160.08 eV for Bi $4f_{5/2}$ and Bi $4f_{7/2}$, respectively, indicate to higher electropositive Bi appearing in the monolayers [4,11]. The XPS peaks of pure Bi_2WO_6 and $0.4CeO_2/0.6Bi_2WO_6$ composite film were found at about 37.00 and 35.00 eV. These refers to W $4f_{5/2}$ and W $4f_{7/2}$ of W^{6+} (high spin) species in Bi_2WO_6 [2,3], as shown in Figure 7.6b. The binding energy of W $4f_{5/2}$ and W $4f_{7/2}$ at about 38.00 and 36.00 eV indicates the oxidation state of W^{5+} (low spin) [5]. The Ce $3d_{5/2}$ and $3d_{3/2}$ peaks of pure CeO_2 and $0.4CeO_2/0.6Bi_2WO_6$ composite film were shown in Figure 7.6c. The binding energy of v, v′′ and v′′′ are located at about 882.00, 888.00 and 898.00 eV, respectively, that is attributed to Ce^{4+} $3d_{5/2}$. The binding energies at about 901.00, 907.00 and 916.00 eV, correspond to u, u′′ and u′′′ of Ce^{4+} $3d_{3/2}$ [6,7]. The Bi 4f, W 4f and Ce 3d peaks of

$0.4CeO_2/0.6Bi_2WO_6$ composite film are shifted to a high binding energy due to stronger chemical bonds in composite [8]. Figure 7.6d shows the binding energy of O 1s of all films. The lattice oxygen in the metal oxides is located the peak at about 529 eV. The peak at 530-531 eV is defined to chemisorbed oxygen or weakly bonded oxygen species. The O1s peaks at binding energies of about 532-536 eV is determined to surface oxygen by hydroxyl species or adsorbed water species on the surface of photocatalyst material [9-11].

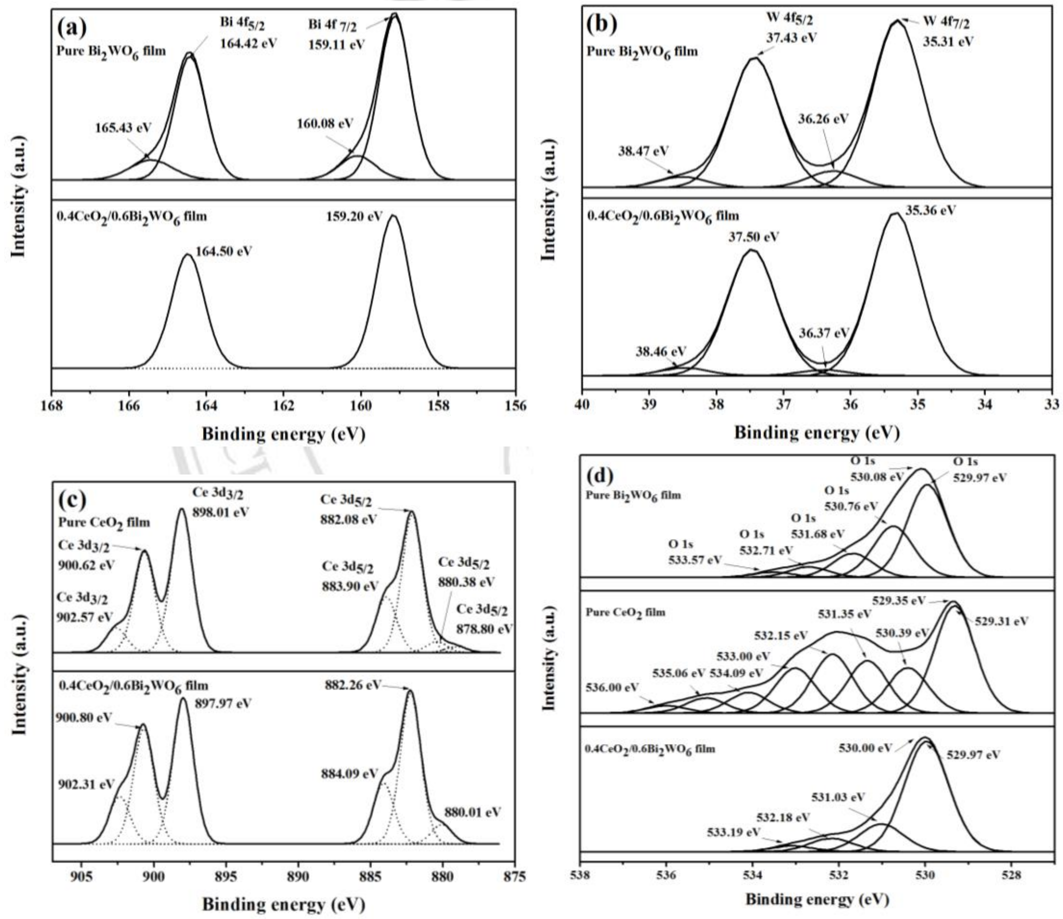

Figure 7.6 XPS spectra of (a) Bi 4f (b) W 4f (c) Ce 3d and (d) O 1s in the three-layered CeO_2, Bi_2WO_6 and $0.4CeO_2/0.6Bi_2WO_6$ composite films.

7.5 UV-vis spectroscopy

The UV-vis spectra of one layer of pure Bi_2WO_6, pure CeO_2 and $0.4CeO_2/0.6Bi_2WO_6$ composite films are presented in Figure 7.7. The absorption peaks of pure Bi_2WO_6, pure CeO_2 and $0.4CeO_2/0.6Bi_2WO_6$ composite films were found to be

418, 459 and 448 nm. The band gaps of pure Bi_2WO_6, pure CeO_2 and $0.4CeO_2/0.6Bi_2WO_6$ composite films were found to be 2.97, 2.70 and 2.77 eV, respectively.

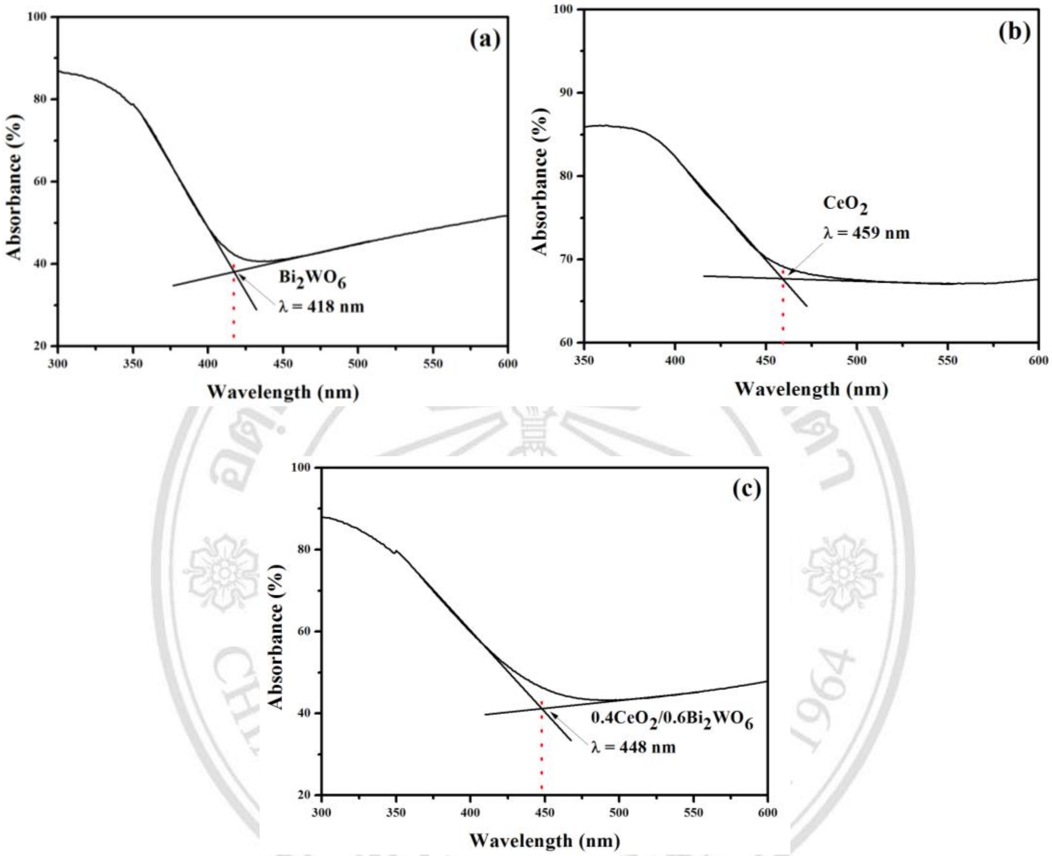

Figure 7.7 The absorption band edge of (a) pure Bi_2WO_6, (b) pure CeO_2 and (c) $0.4CeO_2/0.6Bi_2WO_6$ composite films.

7.6 Photocatalytic activity

All photocatalyst films in one, two and three layers were applied for RhB degradation under visible light irradiation. The photodegradation performance of pure CeO_2, pure Bi_2WO_6 and $0.4CeO_2/0.6Bi_2WO_6$ composite films are exhibited in Figure 7.8. The three layers of $0.4CeO_2/0.6Bi_2WO_6$ composite film were found the highest photoatalytic activity of 44.40%. The *k* value of $0.4CeO_2/0.6Bi_2WO_6$ composite film in 3 layers was established to be 0.00397 min^{-1}. Figure 7.9 displays the comparison photocatalytic efficiency of all samples.

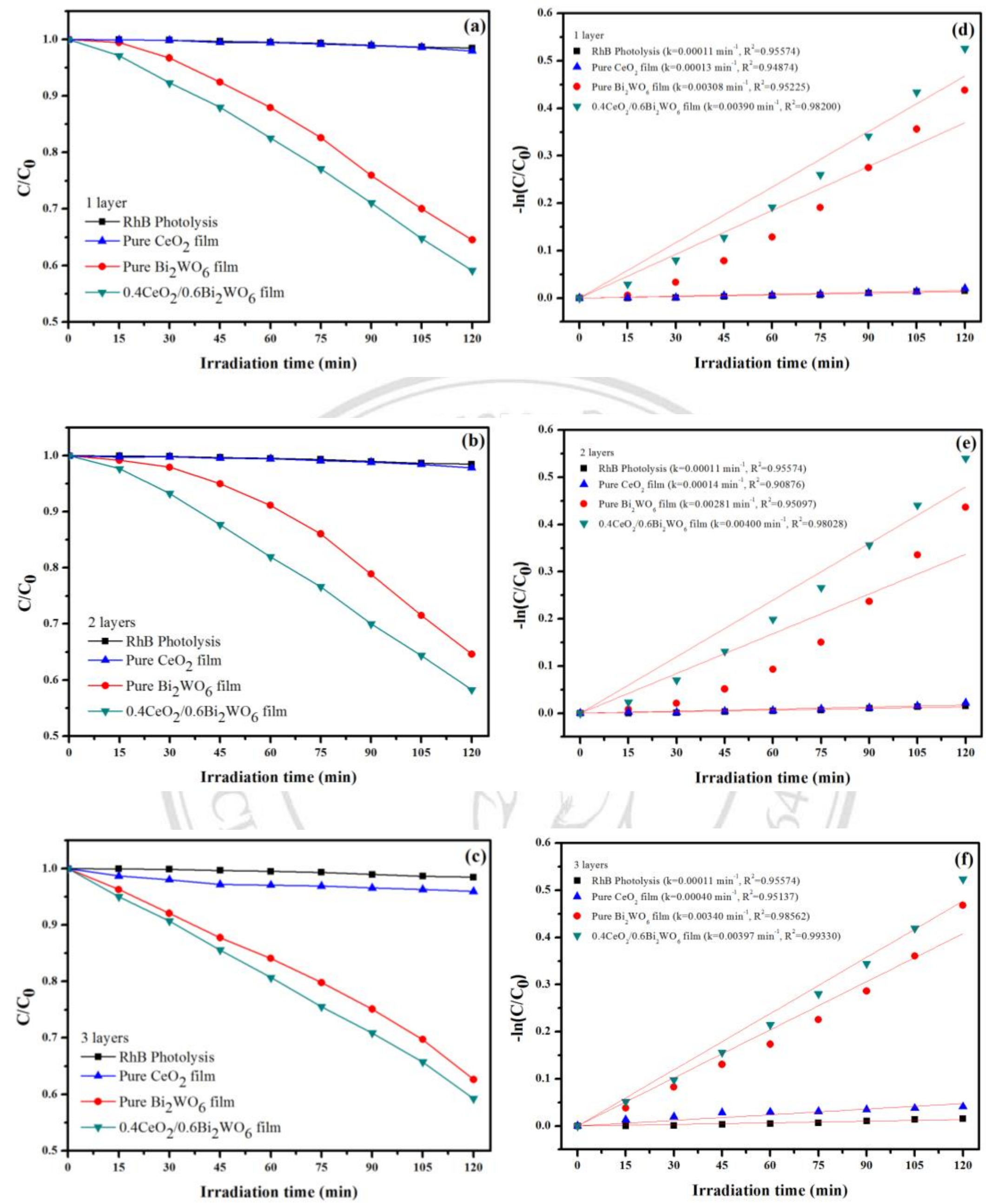

Figure 7.8 Photocatalytic activities and the reaction rate of pure CeO_2, pure Bi_2WO_6 and $0.4CeO_2/0.6Bi_2WO_6$ composite films in one, two and three layers for RhB degradation.

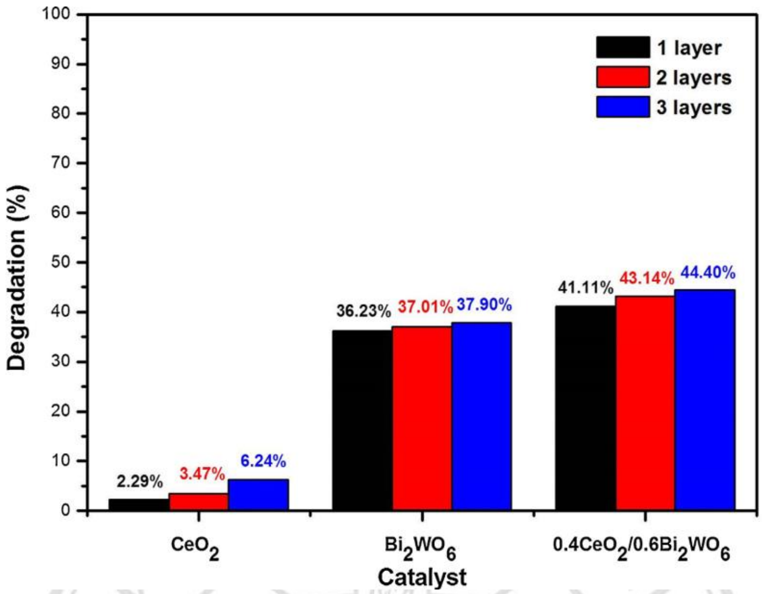

Figure 7.9 The photocatalytic activity comparison of pure CeO_2, pure Bi_2WO_6 and $0.4CeO_2/0.6Bi_2WO_6$ composite films in one, two and three layers for RhB degradation.

7.7 Photocatalytic stability

The photocatalytic stability of three-layered $0.4CeO_2/0.6Bi_2WO_6$ composite film was evaluated by repeating the photocatalytic experiment to confirm the stability efficiency. The circulating runs of three-layered $0.4CeO_2/0.6Bi_2WO_6$ composite film of RhB degradation is presented in Figure 7.10a. Figure 7.10b shows the reaction rate constants (k) of three-layered $0.4CeO_2/0.6Bi_2WO_6$ composite film. The three-layered $0.4CeO_2/0.6Bi_2WO_6$ composite film exhibits the high photocatalytic performance after five recycle runs. The photocatalytic efficiency of $0.4CeO_2/0.6Bi_2WO_6$ composite film for RhB degradation was observed to be 44.23%, 41.05%, 40.74%, 37.49% and 35.67%.

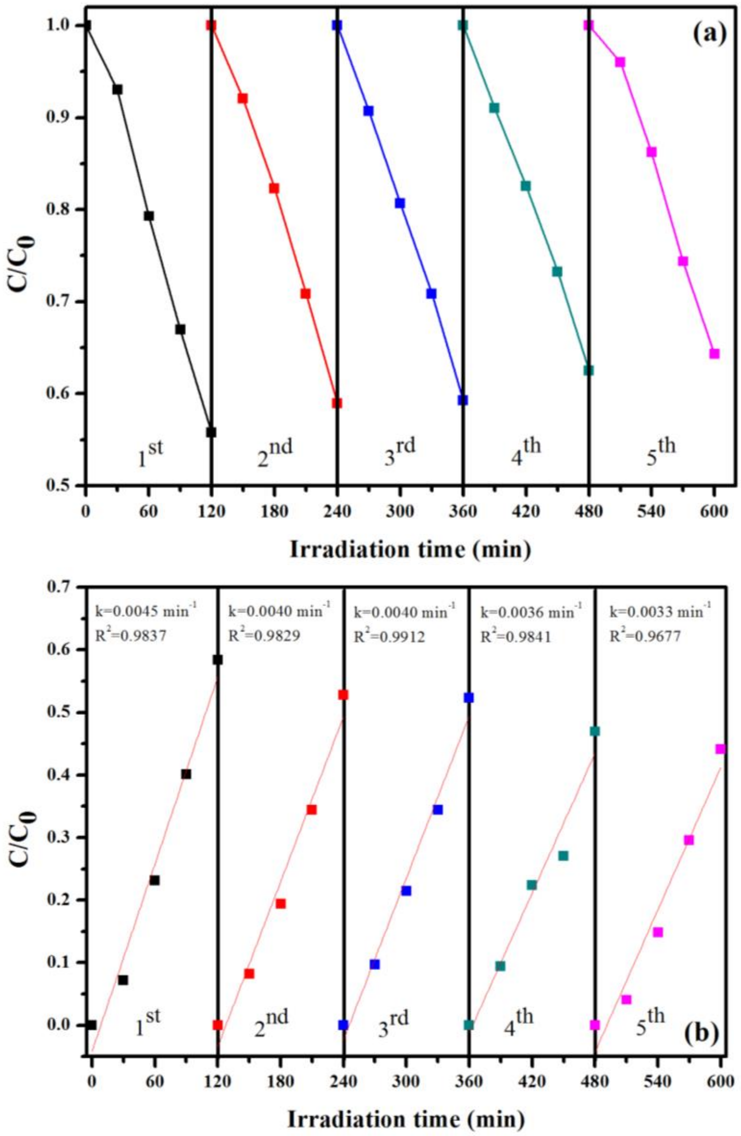

Figure 7.10 (a) the recycling runs of photocatalytic activity and (b) the reaction rate constant of $0.4CeO_2/0.6Bi_2WO_6$ composite films in three layers for RhB degradation.

7.8 Photoluminescence (PL)

Photoluminescence technique was applied to detect the electron-hole pair recombination. Figure 7.11 shows the PL spectra of pure CeO_2, pure Bi_2WO_6 and $0.4CeO_2/0.6Bi_2WO_6$ composite films. The lowest PL intensity was found in the pure CeO_2 film. This implies the low electron-hole pair recombination [12]. Nevertheless, the highest photocatalytic efficiency for degrading RhB was found in $0.4CeO_2/0.6Bi_2WO_6$ composite film. This might be depended on many factors such as size, morphology, and crystallinity of the film.

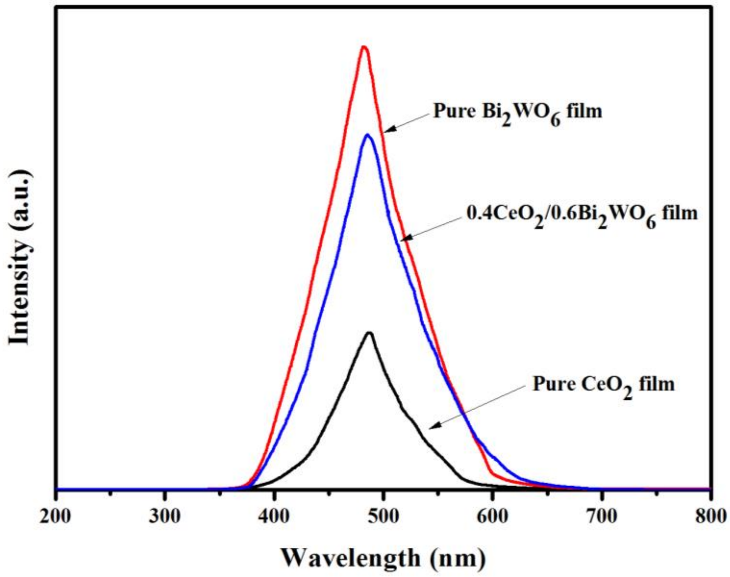

Figure 7.11 The photoluminescence spectra of pure CeO_2, pure Bi_2WO_6 and $0.4CeO_2/0.6Bi_2WO_6$ composite films.

The formation of $\cdot OH$ radicals was measured during the photocatalytic reaction in the RhB solution over the $0.4CeO_2/0.6Bi_2WO_6$ composite film under visible light irradiation. The photoluminescence spectra of 2-hydroxyterephthalic acid were shown in Figure 7.12. The PL peak is increased with increasing irradiation time, implying that the increasing of TA−$OH\cdot$ on the surface of the $0.4CeO_2/0.6Bi_2WO_6$ composite film [8].

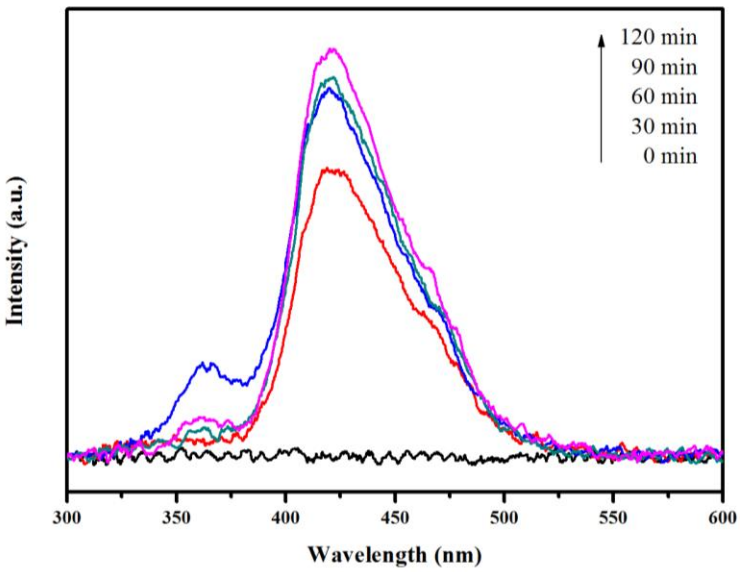

Figure 7.12 The fluorescence spectra of TA−$OH\cdot$ over $0.4CeO_2/0.6Bi_2WO_6$ composite film.

7.9 The photocatalytic mechanism of CeO_2/Bi_2WO_6 composite film

Figure 7.13 presents the photocatalytic mechanism of CeO_2/Bi_2WO_6 composite film. The conduction band of CeO_2 and Bi_2WO_6 were calculated to be –0.28 and +0.38 V, respectively. The valence band of CeO_2 and Bi_2WO_6 were calculated to be +2.42 and +3.35 V, respectively. In photocatalysis process, the electron-hole pair was generated from the activation of photon energy in photocatalyst film. The photogenerated electrons from the conduction band of CeO_2 can transfer to the conduction band of Bi_2WO_6. The photogenerated hole from the valence band of Bi_2WO_6 can transfer to the valence band of CeO_2. The photogenerated electrons are oxidized by oxygen (O_2) to form superoxide anion radical ($\cdot O_2^-$). The photogenerated holes are reduced by H_2O or hydroxyl bond (OH^-) to generate hydroxyl radical ($\cdot OH$). However, the standard redox potentials (E_0) of $O_2/\cdot O_2^-$, $\cdot OH/OH^-$, and $\cdot OH/H_2O$, are located at −0.33, +1.99, and +2.27 V, respectively. The holes in the valence band of CeO_2 and Bi_2WO_6 can be formed hydroxyl radical ($\cdot OH$) by oxidation reaction with OH^- or H_2O because the valence band potentials are more positive than the standard redox potentials of $\cdot OH/OH^-$ and $\cdot OH/H_2O$. Moreover, the electrons in the conduction band of CeO_2 and Bi_2WO_6 cannot react with $\cdot O_2^-$ and $\cdot OH$ because the conduction band potentials are more positive than the standard redox potentials of $O_2/\cdot O_2^-$ [12].

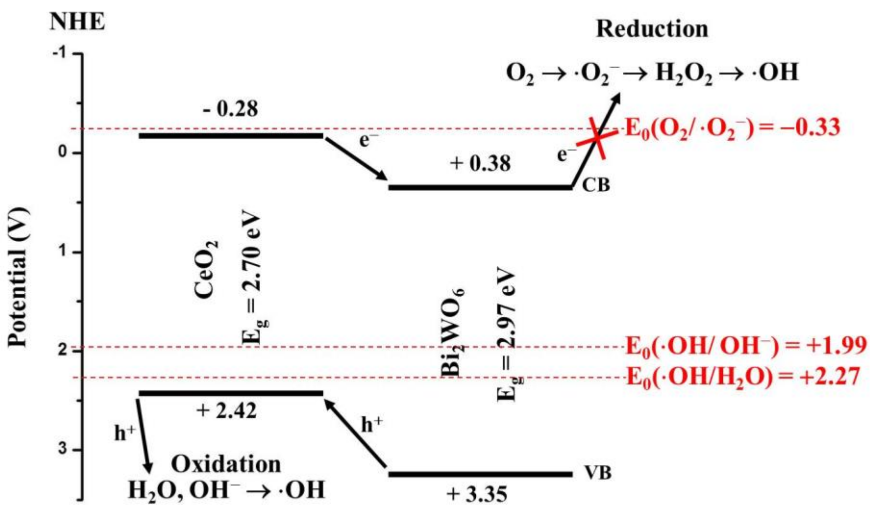

Figure 7.13 The probable photocatalytic mechanism of CeO_2/Bi_2WO_6 composite film.

7.10 Conclusions

The pure CeO_2, pure Bi_2WO_6 and $0.4CeO_2/0.6Bi_2WO_6$ composite films in one, two and three layers were successfully fabricated using a doctor blading method. The crystal structure of CeO_2 and Bi_2WO_6 are cubic fluoride and orthorhombic structure, respectively. The crystallite size of Bi_2WO_6 is bigger than CeO_2. The morphology of CeO_2 shows the spherical-like shape and Bi_2WO_6 presents the plate-like shape. The chemical compositions of $0.4CeO_2/0.6Bi_2WO_6$ composite film consist of Cerium (Ce), Bismuth (Bi), Tungsten (W) and Oxygen (O). The band gap energies of pure Bi_2WO_6, pure CeO_2 and $0.4CeO_2/0.6Bi_2WO_6$ composite films were found to be 2.97, 2.70 and 2.77 eV, respectively. The $0.4CeO_2/0.6Bi_2WO_6$ composite film of 3 layers exhibits the highest photocatalytic activity and stability of RhB degradation for 120 minutes under visible light irradiation. It is expect that the $0.4CeO_2/0.6Bi_2WO_6$ composite film can reduce the recombination of electron-hole pairs, which makes the highest photocatalytic activity. In addition, the $0.4CeO_2/0.6Bi_2WO_6$ composite film promoted the $\cdot OH$ radicals during the photocatalytic reaction.

Table 7.1 The summary of physicochemical properties and photocatalytic efficiency of CeO_2/Bi_2WO_6 composite film.

Properties	**CeO_2 film (3 layers)**	**Bi_2WO_6 film (3 layers)**	**$0.4CeO_2/0.6Bi_2WO_6$ film (3 layers)**
Structure	cubic	orthorhombic	cubic/orthorhombic
Crystallite size	4.30 nm	9.35 nm	6.16 nm
Morphology	sphere-like	plate-like	sphere/plate
Thickness	1.29±0.28 μm	4.37±0.14 μm	4.07±0.70 μm
Band gap	2.70 eV	2.97 eV	2.77 eV
Photocatalytic performance (RhB)	6.24%	37.90%	44.40%

7.11 References

[1] Issarapanacheewin, S. Wetchakun, K. Phanichphant, S. Kangwansupamonkon, W. and Wetchakun, N., “A novel CeO_2/Bi_2WO_6 composite with highly enhanced photocatalytic activity,” Materials Letters, Vol. 156, October 1, 2015, pp. 28-31.

[2] Gui, M. S. Zhang, W. D. Su, Q. X. and Chen, C. H., “Preparation and visible light photocatalytic activity of Bi_2O_3/Bi_2WO_6 heterojunction photocatalysts,” Journal of Solid State Chemistry, Vol. 184, Issue 8, Augusy 2011, pp. 1977-1982.

[3] Duan, F. Zheng, Y. and Chen, M. Q., “Flowerlike $PtCl_4/Bi_2WO_6$ composite photocatalyst with enhanced visible-light-induced photocatalytic activity,” Applied Surface Science, Vol. 257, Issue 6, January 1, 2011, pp. 1972-1978.

[4] Ding, X. Zhao, K. and Zhang, L., “Enhanced photocatalytic removal of sodium pentachlorophenate with self-doped Bi_2WO_6 under visible light by generating more superoxide ions,” Environmental Science and Technology, Vol. 48, April 30, 2014, pp. 5823-5831.

[5] Guo, C. Yin, S. Dong, Q. and Sato, T., “The near infrared absorption properties of $W_{18}O_{49}$,” RSC Advances, Vol. 2, Issue 12, March 5, 2012, pp. 5041-5043.

[6] Anandan, C. and Bera, P., “XPS studies on the interaction of CeO_2 with silicon in magnetron sputtered CeO_2 thin films on Si and Si_2N_4 substrates,” Applied Surface Science, Vol. 283, October 15, 2013, pp. 297-303.

[7] Bêche, E. Charvin, P. Perarnau, D. Abanades, S. and Flamant, G., “Ce 3d XPS investigation of cerium oxides and mixed cerium oxide ($Ce_xTi_yO_z$),” Surface and Interface Analysis, Vol. 40, January 21, 2008, pp. 264-267.

[8] Cui, Y. Li, H. Hong, W. Fan, S. and Zhu, L., “The effect of carbon content on the structure and photocatalytic activity of nano-Bi_2WO_6 powder,” Powder Technology, Vol. 247, October 2013, pp. 151-160.

[9] Liu, H. Wang, M. Wang, Y. Liang, Y. Cao, W. and Su, Y., “Ionic liquid-templated synthesis of mesoporous CeO_2-TiO_2 nanoparticles and their

enhanced photocatalytic activities under UV or visible light," Journal of Photochemistry and Photobiology A: Chemistry, Vol. 223, Issue 2-3, September 25, 2011, pp. 157-164.

[10] Wang, Y. Wang, F. Chen, Y. Zhang, D. Li, B. Kang, S. Li, X. and Cui, L., "Enhanced photocatalytic performance of ordered mesoporous Fe-doped CeO_2 catalysts for the reduction of CO_2 with H_2O under simulated solar irradiation," Applied Catalysis B: Environmental, Vol. 147, April 5, 2014, pp. 602-609.

[11] Zhou, Y. Zhang, Y. Lin, M. Long, J. Zhang, Z. Lin, H. Wu, J. and Wang, X., "Monolayered Bi_2WO_6 nanosheets mimicking heterojunction interface with open surfaces for photocatalysis," Nature Communications, Vol. 6, August 11, 2015, pp. 1-8.

[12] Arul, N.S. Mangalaraj, D. and Kim, T.W., "Photocatalytic degradation mechanism of CeO_2/Tb_2O_3 nanotubes," Applied Surface Science, Vol. 349, September 15, 2015, pp. 459-464.